Direct Imaging of Distorted Vortex Structure and Vortex-Antivortex Mediated Vortex Annihilation In Exchange Coupled Ferromagnetic/ Antiferromagnetic Disk Structures

Arekapudi, S. S. P. K.; Böhm, B.; Ramasubramanian, L.; Ganss, F.; Heinig, P.; Stienen, S.; Fowley, C.; Lenz, K.; Deac, A. M.; Albrecht, M.; Hellwig, O.;

Originally published:

January 2021

Physical Review B 103(2021), 014405

DOI: https://doi.org/10.1103/PhysRevB.103.014405

Direct Imaging of Distorted Vortex Structure and Vortex-Antivortex Mediated Vortex Annihilation In Exchange Coupled Ferromagnetic/Antiferromagnetic Disk Structures

Sri Sai Phani Kanth Arekapudi, Benny Böhm, Lakshmi Ramasubramanian, Fabian Ganss, Peter Heinig, Sven Stienen, Ciarán Fowley, Kilian Lenz, Alina M Deac, Manfred Albrecht, and Olav Hellwig**

Sri Sai Phani Kanth Arekapudi, Benny Böhm, Lakshmi Ramasubramanian, Fabian Ganss, Peter Heinig, Prof. Dr. Olav Hellwig, Magnetic Functional Materials, Institute of Physics, Technische Universität Chemnitz, 09107 Chemnitz, Germany.

Prof. Dr. Olav Hellwig, Lakshmi Ramasubramanian, Dr. Sven Stienen, Dr. Ciarán Fowley, Dr. Kilian Lenz, Dr. Alina M Deac, Institute of Ion Beam Physics and Materials Research, Helmholtz-Zentrum Dresden-Rossendorf, Bautzner Landstrasse 400, 01328 Dresden, Germany.

Prof. Dr. Manfred Albrecht, Institute of Physics, University of Augsburg, Universitätsstraße 1,86159 Augsburg, Germany.

E-mail: phani.arekapudi@physik.tu-chemnitz.de, olav.hellwig@physik.tu-chemnitz.de

Keywords: *Magnetic Vortex, Distorted Vortex Structure, Vortex-Antivortex pairs, Antiferromagnet/Ferromagnet, High-Resolution Magnetic Imaging,*

Abstract

Chiral spin textures, such as skyrmions, merons, and vortices in antiferromagnetic (AFM)/ ferromagnetic (FM) heterostructures, are actively explored for utilization in future data storage and signal processing devices. Here, we present a systematic study of the magnetic vortex structures in soft-magnetic NiFe and exchange coupled NiFe/IrMn and IrMn/NiFe/IrMn disk structures. The annihilation of the magnetic vortex state is mediated by the creation and subsequent annihilation of intermediate V-AV pairs. Using the combination of high-resolution in-field magnetic force microscopy (MFM) and magneto-optic Kerr effect magnetometry, we show a considerable enhancement in the stability of the intermediate V-AV state in exchange coupled NiFe/IrMn and IrMn/NiFe/IrMn disk structures. Analysis of the remanent high-resolution MFM images showed a significant increase in the effective vortex core radius and an additional distortion of the FM vortex structure in exchange coupled disks, most likely

caused by the randomly distributed uncompensated spins at the surface of the AFM layer. We further suggest that the displacement of the vortex core from the center of the disk in exchange coupled disks depends on the magnitude of the exchange bias field and AFM grain properties. Additionally, we present a summary of crucial magnetic vortex properties such as effective core radius, core displacement, handedness, nucleation field, V-AV annihilation field, and interfacial exchange energy in exchange coupled disk structures.

1. Introduction

The interfacial exchange interaction between an AFM and a FM leading to the so-called exchange bias (EB) effect[1] has triggered tremendous interest for its fundamental physics as well as for its impact on applications.[2] It is generally accepted that the uncompensated spins at the surface of the AFM thin film are responsible for pinning the FM,[3,4] leading to the exchange bias field. Heterostructured FM/AFM systems are used in modern spintronics circuits,[5] skyrmion-based spin-torque nano-oscillators,[6] low current density magnetic tunnel junctions (MJT),[7] magnetic vortex-based sensors,[8] and neuromorphic devices.[9] Furthermore, AFM thin films are used to stabilize skyrmions[10] and other chiral spin textures in FMs at zero magnetic field,[11-13] which are proposed as an efficient alternative to the current data storage, transport, and signal processing technologies.[13-16]

Although EB effects in magnetic vortex structures were extensively studied,[17-25] detailed experimental study of vortex-antivortex (V-AV) mediated magnetic vortex annihilation process in FM/AFM[11] and AFM/FM/AFM disk structures are still missing. The topology of the magnetic vortex structure is determined by the in-plane curling in the magnetization around the center, described by the winding number $w = +1$ (for an antivortex $w = -1$).[26-28] The out-of-plane magnetization direction at the center of the core is described by the polarization $p = \pm 1$.[27-29] The topological skyrmion charge of a vortex structure can be parameterized as $q =$

wp/2.[28,30-32] The rotational direction of the local magnetization vector in the plane, either clockwise (CW) or anti-clockwise (ACW), is characterized by the so-called circularity $c = -1$ and +1, respectively.[31,32] The handedness of the vortex is defined by the product $cp = \pm 1$.[31-34] In a magnetic vortex with a lack of symmetry breaking energy contribution known as Dzyaloshinskii-Moriya interaction (DMI), four degenerate ground states can occur with two possible orientations of p and c.[32-36]

The magnetic vortex reversal is mediated by the spontaneous creation and annihilation of a V-AV pairs.[27,37-39] Hertel and Schneider[27] proposed two distinct V-AV pair annihilation mechanisms depending on the relative polarization of the V and AV cores.[28,38] In the first case, with the parallel polarization of the V and AV cores,[37] the total topological skyrmion number of the V-AV pair becomes zero ($q = 0$).[28] Such a topologically trivial V-AV pair can be continuously deformed into a uniform state. In the second case, with antiparallel core polarization of the V and AV pair, the total skyrmions number of the V-AV pair becomes +1 or -1.[27,28] Topologically non-trivial V-AV pair cannot be continuously deformed into a uniform state without involving a point defect (magnetic singularities) referred to as Bloch point (BP).[27,30,37-42] Due to the completely vanishing local magnetization,[30,42] BPs themselves have not been imaged directly. However, imaging the non-trivial magnetic textures such as vortex-domain walls[43] and skyrmions coalescence or separation that supports BPs,[44] combined with the micromagnetic simulations is a generally accepted approach.

In this study, we image the *distorted vortex structure* proposed by Gilbert et al.,[17] in real space, that can occur in exchange coupled FM/AFM disk structures. We study the impact of interfacial exchange coupling between FM (NiFe) and AFM (IrMn) on the V-AV mediated magnetic vortex annihilation process. We further quantify the critical differences between the vortex ground state and V-AV state in FM, FM/AFM, and AFM/FM/AFM disk structures. We employ a combination of in-field high-resolution magnetic force microscopy (Hr-MFM) and magneto-

optical Kerr effect (MOKE) magnetometry with a micro-focused beam, as well as micromagnetic simulations to study the magnetic vortex reversal process. We prepared an array of magnetostatically non-interacting magnetic disk structures with a diameter of 4 μm each and a center-to-center distance (pitch) of 12 μm, made out of soft-magnetic $Ni_{81}Fe_{19}$ (from now on, referred to as NiFe) with a thickness of 40 nm, which is known to yield a low (micromagnetic) energy vortex ground state.[29,32,33,45,51,53] As an AFM, we use $Ir_{30}Mn_{70}$ (referred to as IrMn) 7.5 nm thick.

2. Experimental Section

The disk structures were fabricated on a high resistive commercial p-type Si(100) substrate with a 4 nm thick native SiO_2 layer, using lift-off process. The thin film multilayers were deposited using DC magnetron sputtering with Ar as sputter gas (p_{Ar} = 3 μbar). For all the samples in the study, a Ta (5 nm) seed layer was used to improve the adhesion of the functional materials with the substrate and to promote (111) texture in NiFe thin films. Functional FM and AFM layers were deposited from a 4N purity $Ni_{81}Fe_{19}$ .at% and $Ir_{23}Mn_{77}$ .at % alloy targets at a deposition rate of 0.3 Å/sec. The deposition rates were pre-calibrated by x-ray reflectivity (XRR) measurements and controlled via a quartz microbalance (monitor) during the deposition. Rutherford backscattering spectroscopy (RBS) on sputter-deposited reference thin films revealed the atomic stoichiometry of $Ni_{81}Fe_{19}$ .at% and $Ir_{30}Mn_{70}$ .at%.

In the case of a simple FM disk structure, Pt (2 nm)/Ta (8 nm) bilayer was used as a cap layer. In the remaining samples with the AFM (IrMn) layer, we use Ta (2.5 nm) as a cap layer to protect the functional layers from oxidation. All the samples were designed so that the FM layer is consistently 10 nm below the top surface, which is crucial for a direct comparison of the magnetic contrast obtained from the MFM scans for different samples in the study. Bragg

scans performed using x-ray diffraction revealed a chemically disordered FCC structure with a strong (111) texture for both NiFe (2θ = 44.22°) and IrMn (2θ = 41.12°) layers (see supplementary material S1(a,b and c)). Additionally, we obtain a rocking width of $\Delta\Omega \approx 3.63°$ for NiFe layer and $\Delta\Omega \approx 4.35°$ for the IrMn layer along the (111) orientation (see supplementary material S1(d)).

The field cooling (FC) and zero-field cooling (ZFC) experiments were performed using an MPMS SQUID-VSM with a temperature range of 1.5 K to 1000 K and a maximum magnetic field up to ±7 T. In the FC state, the samples were heated from 300 K to 605 K in a magnetic field of +7 T applied in the film plane, and the samples were kept for 90 min at 605 K (field annealing). Later, the samples were field cooled down to 300 K in +7 T magnetic field. In the ZFC state, after heating the sample to 605 K, the samples underwent an alternating magnetic field cycling, a so-called AC demagnetization routine. Starting from +7 T, we reduce the magnetic field in 3% steps to the negative magnetic field direction and vice-versa (closely following an exponentially decaying triangular function) until the magnetic field reaches close to zero. At zero magnetic field, the samples were annealed for 90 min, followed by the zero-field cooling to 300 K. For consistency, the samples without the AFM layer underwent a similar ZFC demagnetization procedure. The heating and cooling rates were kept constant at 15 K/min for both FC and ZFC procedure. After the FC/ZFC procedure, samples were field cycled between +7 T to -7 T ten times to overcome the training effect,[46,47] prior to the MOKE and MFM measurements.

A commercial nano-MOKE 2 set-up equipped with a He-flow cryostat with a temperature range of 4.5 K to 510 K was used in the study. All the magnetic hysteresis loops shown in the study were obtained in longitudinal geometry with a magnetic field range of ±0.5 T in the film

plane. A red laser with a wavelength of 635 nm and a spot size of <10 μm was used to obtain the hysteresis loops.

In-field high-resolution magnetic force microscopy (Hr-MFM) imaging was performed using the NanoScan MFM. A commercial high-resolution Si tip uniformly coated with a low magnetic moment CoCr alloy operating at a high resonance frequency $f_0 = \omega_0/2\pi$ = 128.515 kHz at an oscillation amplitude of 2.5 nm, and spring constant C = 0.7 N/m was used in the MFM imaging experiments. The measurements were performed in an HV chamber to increase sensitivity and the Q-factor of the tip (>20,000). MFM Scans were performed in non-contact mode while maintaining a constant height of ~10 nm between the dynamically oscillating magnetic tip and the sample surface. The electrostatic potential and the thermal drift between the metallic tip and the sample surface were actively compensated. Within the interaction volume V, the three-dimensional (x, y, z) force component acting on the oscillating magnetic tip due to the magnetic interactions with the stray field of the sample in reciprocal space is given by,[48] $F_Z(n) = -\mu_0 \int M_{FM-tip}(x', y', z') \cdot d/dz' \, H_{sample}[(x', y', z') + r]dV'$, where $M_{FM\text{-}tip}$ is the tip magnetization, $\mu_0 H_{sample}$ is the stray field at the sample surface and $n = (n_x + n_y + n_z)$ is the location of the tip. The highest sensitivity of the tip is to the z' component, which is at the apex of the tip, giving rise to the OOP component of the MFM scan. Away from the apex, which accounts for the x' and y'(IP) components, the sensitivity of the tip drops dramatically. The relative shift in the resonant frequency of the tip due to the force derivative is given by[48,49] $\Delta\omega = \omega_0 \cdot 1/2C \cdot \partial F_Z/\partial z$. An attractive magnetic force gives rise to a negative shift, and a repulsive force gives rise to a positive shift in ω_0. The magnetic field experienced by the magnetic vortex structure during the in-field MFM scan is the vector sum of the static external magnetic field $\mu_0 H_{app}$ and the effective stray field of the tip $\mu_0 H_{tip}$ given by $\mu_0 H_T = \mu_0 H_{app} + \mu_0 H_{tip}$. To achieve magnetic vortex reversal in the hard-axis (OOP)

direction, one would need rather large OOP fields up to $\mu_0 H_K$ = 1.2 T, i.e., the contribution from the non-zero OOP field component originating from the $\mu_0 H_{app}$ and $\mu_0 H_{tip}$ = 12 mT ± 3 mT are neglected (unless stated otherwise).

We carried out a series of micromagnetic simulations using the open-source Mumax3 package.[50] To study the magnetic vortex reversal mediated by the V-AV pair, we consider a disk with 2 µm diameter and 40 nm height, M_S = 800 kA/m, exchange stiffness constant A_{ex} = 1.3 $\times 10^{-12}$ J/m, and uniaxial anisotropy constant K = 0. To further study the role of various material parameters on the static magnetic field stability of V-AV state, we have performed additional simulations considering, $A_{ex} = 1.3\times10^{-11}$ J/m and 1.0×10^{-11} J/m, and K = 0, 0.2×10^3 J/m^3 and 0.4 × 10^3 J/m^3. We choose 1×1×40 nm^3 and 2×2×40 nm^3 cell-sizes for 1 µm and 2 µm disk structures, respectively. In the supplementary Table S1 and S2, we present a summary of material parameters as well as the obtained exchange energy for the vortex state and the V-AV states.

3. Results and discussion

The magnetic vortex annihilation mediated by the creation and annihilation of the V-AV pairs obtained from the micromagnetic simulation is shown in Figure 1a-1f. Upon applying a static magnetic field along the x-direction, the initial motion of the core is determined by the vortex handedness $c{\cdot}p$.[31] For $c{\cdot}p$ = +1, the core moves orthogonally towards the positive y-direction, as shown in figure 1b and 1c. The vortex handedness $c{\cdot}p$ = -1 results in the motion of the core towards the negative y-direction. Due to the competition between the magnetostatic energy and the Zeeman energy, the core is deflected from the center of the disk to increase the area with magnetic moments aligned parallel to the applied magnetic field direction.[51] The vortex state remains intact, as shown in figure 1c. For small core displacement from the center of the disk, the exchange energy remains almost unchanged (see supplementary Figure S2 b(ii)). At a

critical applied magnetic field, the V-AV pairs are created to assist the annihilation of the magnetic vortex[37,39] at the expense of exchange energy. The formation of the V-AV pairs causes a buckling of the spin texture, as shown in figure 1d. Increasing the magnetic field further results in the annihilation of the V-AV pairs accompanied by the spontaneous decay of exchange energy.[27] Once the V-AV pairs are annihilated, an edge state is formed, followed by the saturation of the disk, as shown in Figure 1e and 1f, respectively. Edge state is characterized by two vortex cores at the left and the right edge of the disk with opposite core polarization. For detailed in-plane (IP) and out-of-plane (OOP) magnetization component of the vortex state, V-AV and edge state, as well as the micromagnetic energy terms as a function of the applied magnetic field for various material parameters, see supplementary Figure S2, S3, and S4.

Figure 1g shows the spin structure of V-AV pairs overlaid on the buckled IP magnetic contrast. To understand the elusive creation and annihilation mechanism of V-AV pairs, we consider a simple V-AV-A triplet. The initial vortex V_1 with polarization p = +1 and a newly created vortex V_2 with opposite polarization p = -1, separated by an antivortex core with p = -1 as shown in figure 1h. Due to the antiparallel polarization of the vortex (V_1) and AV cores,[37,39] the total topological skyrmion charge $q_{\text{V-AV}}$ of the V_1-AV pair adds to a total of +1.[28] The creation and annihilation of such a topologically non-trivial V-AV pair require a spontaneous injection of the magnetic point defects such as BPs[27,28,30,37-42] at the top or the bottom surface of the FM film at the expense of exchange energy.[27,52] A BP can be described as a three-dimensional topological invariant singularity of the magnetization field vector, where the local magnetization completely vanishes (in-plane magnetization $m_x = m_y = 0$ and OOP magnetization $m_z = 0$).[30,40-42] The structure of the spiraling BP shown in Figure 1h can be obtained from the hedgehog solution,[30,42] where the magnetic moments around the unit sphere are rotated by an angle >90° to reduce the magnetostatic energy (see supplementary Figure S5).

The spiraling BP configuration supports the V-AV pair with opposite core polarization[42]. Once the BPs propagate through the film thickness in the OOP direction, the V-AV pairs are annihilated, and an edge vortex state is formed. If we were to assume a parallel polarization of the V_1-AV cores,[37] the total topological skyrmion charge ($q_{V\text{-}AV}$) becomes zero.[28] Such a V-AV spin texture can be continuously deformed into a uniform state without invoking the BPs.[28,31,37]

The characteristic length scale l_{BP} of a BP similar to the one shown in figure 1h is predicted to be far below the exchange length l_{ex} of a given magnetic material.[30] The exchange length[52,53] of the NiFe (40 nm) reference thin film $l_{ex} = \sqrt{2A_{ex}/\mu_0 M_s^2}$ =5.8 nm, where A_{ex} = 1.28×10^{-11} J/m is the exchange stiffness constant determined from the perpendicular standing wave (PSSW) modes using ferromagnetic resonance (FMR) spectroscopy. The saturation magnetization M_s = 778 kA/m, as determined by SQUID-VSM magnetometry.

We now reproduce the magnetic vortex annihilation mediated by the V-AV pairs experimentally in the disk structures shown in figure 2a, 2b, and 2c for FM: NiFe (40 nm), FM/AFM: NiFe (40 nm)/IrMn (7.5 nm) and AFM/FM/AFM: IrMn (7.5 nm)/NiFe (40 nm)/IrMn (7.5 nm) multilayers, respectively. In the simple FM disk structure shown in figure 2a, we obtain a magnetic hysteresis loop in longitudinal geometry upon applying an in-plane magnetic field, as shown in Figure 2d. The inset shows the full hysteresis loop, which is characteristic of the presence of a magnetic vortex state.[51,53] From the descending branch of the MOKE hysteresis loop, we obtain the nucleation field of the FM vortex core $\mu_0 H_n$ = 14 mT $\pm$ 1 mT, accompanied by an abrupt reduction in the magnetization. The in-field MFM measurements were performed in the ascending branch of the hysteresis loop, as indicated by the black arrowheads in figure 2e. The remanent magnetic vortex structure is shown in Figure 2g(i). The in-field MFM images corresponding to the V-AV mediated magnetic vortex annihilation are shown in figure 2g(ii-vi). Due to the product $c \cdot p$ =(+1)·(+1) = +1, the vortex

core continuously deflects orthogonal in the positive *y*-direction in the film plane with respect to the magnetic field normal in the positive *x*-direction, as shown in figure 2g(i and iii). As mentioned earlier, to assist the magnetic vortex annihilation process, V-AV pairs are formed at a critical field of about 16 mT ± 1 mT. The MFM image corresponding to the *buckled state* is shown in Figure 2g(iv). In the next step, we increase the applied magnetic field $\mu_0 H_{app}$ only by around 2 mT. As a result, V-AV pairs are annihilated, forming an edge state shown in figure 2g(v). When the magnetic field reaches the saturation field, the FM disk stabilizes in a single-domain (saturated) state (see Figure 2g(vi)). After the saturation of the FM disk, decreasing the magnetic field to zero resulted in the reversal of the vortex core polarization (p = -1, q = -1).

We repeated the in-field MFM measurement to determine the static magnetic field stability of the V-AV state in the FM disk. The buckled (V-AV) spin structure reappeared at $\mu_0 H_{app} \approx +15$ mT ± 1 mT (see Figure 2g(iv)). By repeating the MFM scan (keeping the $\mu_0 H_{app}$ constant at +15 mT), the V-AV state degenerated into the edge state, which indicates a somewhat unstable (volatile) nature of the V-AV state. The stray field of the magnetic tip ($\mu_0 H_{tip}$) that the disk is exposed to during the scan is sufficient to annihilate the V-AV pairs.[78]

To further understand the V-AV mediated magnetic vortex annihilation mechanism and the stability of the V-AV pairs in a static magnetic field, we performed a series of micromagnetic simulations. We considered the exchange stiffness constant similar to the experimental values $A_{ex} = 1.3\times10^{-11}$ J/m and 1.0×10^{-11} J/m and $K = 0$, 0.2×10^{3} J/m^3 and 0.4×10^{3} J/m^3. Surprisingly, the V-AV state is not stable in the static magnetic field regime. The vortex state spontaneously decays into an edge state, as shown in Supplementary Figure S2(a). Once the BPs are injected at the surface of the FM disk to assist the creation of the topologically non-trivial V-AV pairs, they tend to spontaneously propagate through the film thickness in the OOP direction, resulting

in the annihilation of the V-AV pairs.[27,30,39,54] Increasing the uniaxial anisotropy of the NiFe thin film in the micromagnetic simulations[23] (e. g., K = 0, 0.2×10^3 J/m^3 and 0.4 × 10^3 J/m^3) did not stabilize the V-AV pairs. In contrast, we were able to image the V-AV state in the NiFe disks as shown in figure 2g(iv). Kim and Tchernyshyov[30] proposed a theoretical mechanism of pinning the BPs by the inevitable lattice defects/imperfections in the FM thin films. As BPs are scale-invariant ($l_{BP} \ll l_{ex}$), it is conceivable that the spatially varying magnetization of the propagating BP can be pinned by the face-centered cubic (fcc) lattice defects/imperfections along with the thickness of the film (in the OOP direction).[30] Such a mechanism of pinning the BPs can stabilize the intermediate V-AV pairs from degeneracy for a limited magnetic field range.

Alternatively, we consider A_{ex} = 1.3×10^{-12} J/m in the micromagnetic simulations. As a result, we observed a significant increase in the magnetic field stability of the V-AV pairs. The exchange energy for the vortex state and the V-AV state and various geometric and material parameters considered in the micromagnetic simulations are listed in supplementary table S1 and S2. Experimentally, tuning the A_{ex} of NiFe alloys is beyond the scope of this work. For example, Ruslan *et al*. [55] showed that it is possible to tune the A_{ex} of $(Ni_{81}Fe_{19})_{100-x}Gd_x$ alloy thin films by systematically varying the Gd at.%.

Increasing the static magnetic field stability of the V-AV pairs (or 1-D domain walls) are highly desirable for spintronic and magnonic applications. Non-trivial spin textures such as V-AV domain walls are shown to overcome the Walker-breakdown limit.[56] Thus significantly increasing the operating frequency range of the domain wall-based devices.[56-58] Due to the intrinsic and dynamic nature of the BP mediated V-AV state,[27,39,54] thus far, it was not possible to extend the magnetic field range of BP mediated V-AV state without significantly changing the geometry of the magnetic micro or nanostructures.[59,60] For example, in soft-magnetic elliptical (stadium shaped) nanostructures, V-AV-V triplet structures can be stabilized at zero

magnetic field.[60] Alternatively, using the interfacial exchange coupling between the FM and the AFM layer in circular disk-shaped structures, we show that it is possible to extend the static magnetic field stability of the intermediate V-AV state.

We now turn the attention to the exchange coupled FM/AFM disk structures shown in figure 2b, where an AFM-IrMn (7.5 nm) layer is introduced at the top surface of the NiFe (40 nm) disk structure. A longitudinal MOKE hysteresis loop for the exchange coupled FM/AFM: NiFe (40 nm)/IrMn (7.5 nm) disk structure after the FC process is shown in Figure 2e. We extract the EB field $\mu_0 H_{eb}$ = -2.5 mT from the loop shift of full MOKE hysteresis loop shown as an inset in figure 2e. Due to the inverse scaling of $\mu_0 H_{eb}$ with respect to the FM film thickness t_{FM} ($\mu_0 H_{eb} \propto 1/t_{FM}$),[1,61] we expect a small loop shift. From the descending branch of the MOKE hysteresis loop, we obtain the nucleation field[17] of the exchange biased vortex core $\mu_0 H_n$ = 18 mT $\pm$ 1 mT. The in-field MFM measurements were performed in the ascending branch of the hysteresis loop, as indicated by the black arrowheads in Figure 2e. The remanent and in-field MFM images for the exchange coupled *disk 1* ($c \cdot p$ = -1) and *disk 2* ($c \cdot p$ = +1) are shown in Figure 2h and 2i, respectively.

At remanence for *disk 1,* we observe that the core is deflected in the negative *y*-direction by about 270 nm from the disk center (orthogonal with respect to the cooling field $\mu_0 H_{FC}$ direction), as shown in Figure 2h(i). However, in *disk 2* shown in figure 2i(i), for the same $\mu_0 H_{FC}$ direction, the core is deflected in the positive *y*-direction by about 210 nm from the center of the disk. The displacement of the vortex core position from the center of the exchange coupled FM/AFM disks (so-called *tilted vortex*[17,21,22]) depends on the magnitude of the exchange bias field,[17,18,21-23] and the local AFM disorder.[17,63] In contrast, the direction of deflection in either positive or negative *y*-direction is determined by the handedness of the vortex structure.[23,24] The handedness (or chirality) protection in exchange coupled FM/AFM disks and thin films were addressed in earlier studies.[23,24,68] In the exchange coupled FM/AFM

disks, the competition between the radial spin alignment of the FM vortex structure and the sporadically canted (non-planar) spin structure of the polycrystalline AFM,[64,65] in addition to the orange peel coupling[66,67] resulted in a radial star-like pattern with spatially alternating contrast, which we call a *distorted vortex structure*.[17] Moreover, the evolution of the FM vortex structure is correlated to the randomly distributed uncompensated spins at the surface of the AFM layer.[79,80] Additionally, remanent MFM experiments on FM/AFM disk structures as a function of AFM film thickness t_{AFM}, revealed that the *distorted vortex structure* is present in FM/AFM disks with t_{AFM} >4.0 nm, which is generally associated with the AFM film thickness dependent onset of the EB field.[17,21,22,61,62] A *tilted vortex structure*[21] is only observed in disks with $t_{AFM} \geq 6.0$ nm.

The V-AV mediated magnetic vortex annihilation process for exchange coupled FM/AFM *disk 1* and *2* are shown in figure 2h(ii-vi) and 2i(ii-vi), respectively. The V-AV state was stable for both *disk 1* and *2* between 18 mT to 26 mT $\pm$ 1 mT. From the ascending branch of the MOKE hysteresis loop and the in-field MFM study, we obtain the V-AV annihilation field $\mu_0 H_a \approx 28$ mT $\pm$ 1 mT. In comparison, the V-AV state was volatile ($\mu_0 H_a \approx 15$ mT $\pm$ 1 mT) in the FM disks. We observed an increase in the V-AV state stability field range to ~8 mT $\pm$ 1 mT in the exchange coupled FM/AFM disks (see supplementary movie 1).

For the AFM/FM/AFM disk structure shown in figure 2c, the characteristic MOKE hysteresis loop for FC and ZFC state are shown in Figure 2f. In the FC state, a definite shift in the vortex hysteresis loop by $\mu_0 H_{ex}$ = -4.5 mT is detectable, whereas no loop shift is present after the ZFC procedure. Due to the presence of randomly distributed uncompensated spins at the surface of the bottom and the top AFM layers,[71,72,79,80] we see an additional enhancement in the magnetic field stability of the V-AV state (up to 11 mT) in both FC and ZFC state. This becomes apparent in the ascending branch of the MOKE hysteresis loop shown in Figure 2f, where an intermediate plateau is present (indicated by the brown-colored dashed line). From the

descending branch of the MOKE hysteresis loops shown in Figure 2f, we obtain $\mu_0 H_n \approx 14$ mT $\pm$ 1 mT and 18 mT $\pm$ 1 mT in the FC and ZFC states, respectively. The remanent and in-field MFM image sequence for the AFM/FM/AFM disk structure is shown in Figure 2j. The AFM/FM/AFM disks were field cooled in the positive *x*-direction. Due to the vortex handedness $c \cdot p = +1$, we see a deflection of the vortex core from the center of the disk in the positive *y*-direction by about 160 nm. Similar to the FM/AFM disks, we observe a distorted vortex structure at remanence in AFM/FM/AFM disk structure (see figure 2j(i)). We reproduce the V-AV mediated magnetic vortex annihilation process as shown in figure 2j(ii-vi), where we obtain the V-AV annihilation field $\mu_0 H_a \approx 27$ mT $\pm$ 1 mT and 31 mT $\pm$ 1 mT for the FC and ZFC states, respectively.

We carried out additional in-field MFM measurements on FM/AFM and AFM/FM/AFM disks to check the stability and reproducibility of the V-AV state. In both cases, the V-AV state remained intact even after repeated in-field MFM scans. To examine the stability of the V-AV state over time, we kept the $\mu_0 H_{app} = +26$ mT for more than 24 hours and performed an additional MFM scan. The V-AV state shown in Figure 2h(iv), 2i(iv) and 2j(iv) remained intact. The uncompensated spins at the FM/AFM interface[71,72,79,80] are not able to pin the BPs directly, as they tend to propagate along the OOP direction.[30,69] However, uncompensated spins can pin the buckled (V-AV) spin texture at the FM/AFM interface,[70-72,79,80] whose local pinning potential[73] can be substantial. The applied magnetic field must overcome the interfacial exchange bias field experienced by the V-AV spin structures originating from the FM/AFM interface[70-72] and the pinning force in the OOP direction experienced by the BPs due to crystal defects.[30] Therefore, we see an increase in the magnetic field stability of the intermediate V-AV state in exchange coupled FM/AFM and AFM/FM/AFM disk structures.

We now address the critical differences between the remanent vortex state and the V-AV state observed in the samples with and without the AFM layers by analyzing the corresponding line

profiles, as shown in Figure 3. We have extracted the effective vortex core radius $r_{eff} \approx 70$ nm from the half-width at half maximum (HWHM) of the line profile shown in figure 3a for the FM disk.[74] The r_{eff} extracted from the line profile of the MFM scans can significantly deviate from the true magnetic vortex core radius r_c, most likely due to the instrument broadening.[29,75] Therefore, we provide a numerical estimate of the minimum vortex core radius[75,76] $r_c = (l_{ex}^2 R/12\kappa\beta)^{1/3} \approx 14$ nm, $R = 2$ μm is the radius of the disk, $\kappa = 4.12\times10^{-2}$ is the numerical constant,[75] $L = 40$ nm is the height of the disk, and $\beta = 50$ is the ratio of R/L. The numerical estimate $r_c \approx 2.41 l_{ex}$ is in decent agreement with the previous experimental values.[76] The significant broadening of $r_{eff} \approx 5r_c$ in the MFM experiments can be explained by considering various extrinsic contributions such as scan height and the shape of the tip apex.[48,74,77] For instance, decreasing the scan height can reduce the deviation between r_{eff} and r_c to a certain degree.[77] However, the stray fields from the dynamically oscillating magnetic tip can significantly displace and modify the vortex core,[78] which puts a lower limit on the scan height.

The MFM scans for the FM, FM/AFM, and AFM/FM/AFM disk structures in the study were performed using the same magnetic tip while maintaining a constant scan height of ~10 nm between the top surface of the disk and the magnetic tip, in addition to the cap layer and/or AFM layer thickness of ~10 nm. The total distance between the dynamically oscillating tip and the FM layer is maintained at ~20 nm in all three cases. Therefore, the r_{eff} extracted from the core profile in the study for various disk structures provides a decent measure of the relative changes. Consistently, we detect an increase in the r_{eff} for exchange coupled disk structure as shown in Figure 3c, 3e, and 3g.

We observed a significant magnetic contrast corresponding to the vortex sideband shown in Figure 3a, 3c, 3e, and 3g. The MFM scans obtained in non-contact (NC) mode are free of

topographic interference.[48,79,80] If the observed vortex sideband contrast at remanence shown in Figure 3a, 3c, 3e, and 3g is of topographic origin, these features should also be present in the saturated magnetic disk. Unlike magnetostatic interactions, topographic features resulting from the van der Waals interactions between the magnetic tip and the sample are independent of the applied external magnetic field ($\mu_0 H_{app}$).[48,79,80] In the case of the simple FM disk shown in Figure 3a, due to the high sensitivity of the instrument, we detect a weak vortex sideband contrast. This sideband contrast can be attributed to the magnetic inhomogeneities and/or orange peel coupling,[66,67] that shows the tendency of the FM spins at the surface (or surface charges) to follow the surface morphology. In exchange coupled disk, the strong antiferromagnetic coupling between the randomly distributed (non-planar) uncompensated spins of the AFM[79,80] and the in-plane component of the FM vortex structure, in addition to the orange peel coupling, lead to a significant enhancement of the vortex sideband contrast (see Figure 3c, 3e, and 3g).

The magnetic contrast (Δf (Hz)) corresponding to the buckled (V-AV) spin texture is relatively weak in the simple FM case, as shown in Figure 3b. However, in exchange coupled FM/AFM and AFM/FM/AFM disks, an enhanced magnetic contrast for the buckled spin texture is observed (highlighted with a black-colored dashed rectangle in Figure 3h). We have used the same scan height and magnetic tip for scanning the three samples shown and discussed in the study. It allowed us to attribute the enhanced magnetic contrast to a non-planar interfacial spin structure of the AFM,[64,65] which tilts the FM buckled spin structure more towards the OOP direction via interfacial exchange coupling.[79,80]

To understand the increase in r_{eff} and the magnetic contrast corresponding to the buckled spin texture in exchange coupled FM/AFM and AFM/FM/AFM disk structures, we must understand the spin order of the AFM γ-IrMn layer. Bragg scans obtained from x-ray diffraction measurements confirm a chemically disordered γ-$IrMn_3$ phase, with a strong (111) texture (see

supplementary Figure S1). For the chemically disordered γ-$IrMn_3$ phase, below the Néel temperature T_N, the Mn moments in the fcc crystal lattice are tilted by >45° from the diagonal axis towards the cubic faces, as determined by neutron diffraction experiments.[65] In such a case, the FM spins at the FM/AFM interface prefer a tilted alignment towards the OOP direction. Therefore, we see an increase in r_{eff} and magnetic contrast corresponding to the V-AV state for the exchange coupled FM/AFM and AFM/FM/AFM disk structures.

In Table 1, we present a summary of crucial characteristic magnetic vortex properties in the simple FM disks and compare them to the vortex structures observed in the FM/AFM and AFM/FM/AFM disks. In the exchange coupled FM/AFM and AFM/FM/AFM vortex structures, r_{eff}, and the deflection of the vortex core position from the center of the disk Δd_{core} is significantly larger compared to the FM case. Due to the somewhat random nature of the local grain properties (disorder) of the AFM layer,[63] r_{eff} and Δd_{core} do not show a clear monotonic dependence on the interfacial exchange energy ΔE_{eb}. Additionally, from the line profile of the buckled spin textures shown in figure 3(b,d,f, and h), we extract the number of V-AV pairs formed in the FM, FM/AFM, and AFM/FM/AFM disk structures. We found a significant increase in the V-AV annihilation field in the exchange coupled FM/AFM and AFM/FM/AFM disk structures. The increase in the stability range of the V-AV state in exchange coupled disk structures is correlated to the increase in ΔE_{eb}.

Conclusion:

In summary, we have systematically studied the remanent vortex structure and V-AV mediated magnetic vortex annihilation processes in NiFe (40 nm), NiFe (40 nm)/IrMn (7.5 nm) and IrMn (7.5 nm)/NiFe (40 nm)/IrMn (7.5 nm) disk structures. In exchange coupled FM/AFM and AFM/FM/AFM disks, the distortion of the FM vortex structure is correlated to the randomly distributed non-planar uncompensated spins at the surface of the polycrystalline AFM layer.

Analysis of the remanent high-resolution MFM images revealed a considerable increase in the effective vortex core radius in exchange coupled disks. The deflection of the vortex core from the center of the exchange coupled disks at remanence depends on the magnitude of the exchange bias field and the AFM grain properties. At remanence, the direction of the vortex core deflection with respect to the cooling field orientation depends on the handedness of the exchange biased vortex structure. Detailed in-field MFM and MOKE magnetometry study of V-AV mediated magnetic vortex annihilation processes in FM, FM/AFM, and AFM/FM/AFM disk structures revealed a significant increase in the magnetic field stability of the intermediated V-AV state in exchange coupled disks. Our experimental study of crucial magnetic vortex properties in FM, FM/AFM, and AFM/FM/AFM disk structures provide a deeper understanding of the interfacial exchange interaction between the FM vortex structure and a polycrystalline chemically-disordered AFM layer.

Acknowledgments**:** Authors would like to thank Prof. Georgeta Salvan for facilitating access to the nano-MOKE2 set-up, Prof. Christoph Tegenkamp, for providing access to the SEM facilities at TU Chemnitz and technical support from Miriam Lenz at the HZDR facilities. Additionally, the authors would like to acknowledge discussions with Dr. Jürgen Lindner from HZDR and Dr. Sebastian Wintz from PSI.

Conflicts of interest:

The authors declare no conflict of interest.

References

[1] W. H. Meiklejohn and C. P. Bean., *Phys. Rev*. 102:1413 (1956).

[2] J. Železný, P. Wadley, K. Olejník, A. Hoffmann, H. Ohno, *Nature Phys*. 14, 220–228 (2018).

[3] M. Bode, E. Y. Vedmedenko, K. von Bergmann, A. Kubetzka, P. Ferriani, S. Heinze, R. Wiesendanger, *Nature Mater*. 5, 477–481 (2006).

[4] T. Kosub, M. Kopte, R. Hühne, P. Appel, B. Shields, P. Maletinsky, R. Hübner, M. O. Liedke, J. Fassbender, O. G. Schmidt, D. Makarov, *Nat. Commun*. 8, 13985 (2017).

[5] S. Fukami, C. Zhang, S. DuttaGupta, A. Kurenkov, and H. Ohno, *Nature. Mater*. 15, 535 (2016).

[6] F. Garcia-Sanchez, J. Sampaio, N. Reyren, V. Cros, J-V. Kim, *New J. Phys*. 18, 075011 (2019).

[7] A. Chanthbouala, R. Matsumoto, J. Grollier, V. Cros, A. Anane, A. Fert, A. V. Khvalkovskiy, K. A. Zvezdin, K. Nishimura, Y. Nagamine, H. Maehara, K. Tsunekawa, A. Fukushima, S. Yuasa, *Nature Phys*. volume 7, pages 626–630 (2011).

[8] D. Suess, A. Bachleitner-Hofmann, A. Satz, H. Weitensfelder, C. Vogler, F. Bruckner, C. Abert, K. Prügl, J. Zimmer, C. Huber, S. Luber, W. Raberg, T. Schrefl & H. Brück1, *Nat. Electron*. 1, 362–370 (2018).

[9] J. Grollier, D. Querlioz, K. Y. Camsari, K. Everschor-Sitte, S. Fukami, M. D. Stiles, *Nat. Electron.* (2020). https://doi.org/10.1038/s41928-019-0360-9.

[10] G. Yu, A. Jenkins, X. Ma, S. A. Razavi, C. He, G. Yin, Q. Shao, Q. L. He, H. Wu, W. Li, W. Jiang, X. Han, X. Li, A. C. B. Jayich, P. K. Amiri, K. L. Wang, *Nano Lett*. 18, 980 (2018).

[11] F. P. Chmiel, N. Waterfield Price, R. D. Johnson, A. D. Lamirand, J. Schad, G. van der Laan, D. T. Harris, J. Irwin, M. S. Rzchowski, C.-B. Eom, P. G. Radaelli, *Nature Mater* 17, 581–585 (2018).

[12] Albisetti, E.; Calò, A.; Spieser, M.; Knoll, A.W.; Riedo, E.; Petti, D. *Appl. Phys. Lett*. 113, 162401 (2018).

[13] D. Mitin, A. Kovacs, T. Schrefl, A. Ehresmann, D. Holzinger, M Albrecht, *Nanotechnology* 29, 355708 (2018).

[14] E. Albisetti, D. Petti, M. Pancaldi, M. Madami, S. Tacchi, J. Curtis, W. P. King, A. Papp, G. Csaba, W. Porod, P. Vavassori, E. Riedo & R. Bertacco, *Nature Nano*. 11, 545–551 (2016).

[15] Edoardo Albisetti, Daniela Petti, Giacomo Sala, Raffaele Silvani, Silvia Tacchi, Simone Finizio, Sebastian Wintz, Annalisa Calò, Xiaorui Zheng, Jörg Raabe, Elisa Riedo & Riccardo Bertacco. *Communications Physics* 1, 56 (2018)

[16] Albisetti, E., Tacchi, S., Silvani, R., Scaramuzzi, G., Finizio, S., Wintz, S., Rinaldi, C., Cantoni, M., Raabe, J., Carlotti, G., Bertacco, R., Riedo, E. and Petti, D., *Adv. Mater*. 32, 9 (2020).

[17] Dustin A. G., L. Ye, A. Varea, S. Agramunt-Puig, N. Valle, C. Navau, J. F. López-Barbera, K. S. Buchanan, A. Hoffmann, A. Sánchez, J. Sort, K. Liu, J. Nogués, *Nanoscale* 7, 9878–9885 (2015).

[18] J. Sort, A. Hoffmann, S.-H. Chung, K. S. Buchanan, M. Grimsditch, M. D. Baró, B. Dieny, and J. Nogués, *Phys. Rev. Lett*. 95, 067201 (2005).

[19] J. Sort, G. Salazar-Alvarez, M. D. Baró, B. Dieny, A. Hoffmann, V. Novosad, J. Nogués, *Appl. Phys. Lett.* 88, 042502 (2006).

[20] J. Sort, K. S. Buchanan, V. Novosad, A. Hoffmann, G. Salazar-Alvarez, A. Bollero, M. D. Baró, B. Dieny, and J. Nogués, *Phys. Rev. Lett.* 97, 067201 (2006).

[21] K. Yu. Guslienko, A. Hoffmann, *Phys. Rev. Lett*. 97, 107203 (2006).

[22] K. Y. Guslienko and A. Hoffmann , *J. Appl. Phys.* 101 , 093901 (2007)

[23] M. Tanase, A. K. Petford-Long, O. Heinonen, K. S. Buchanan, J. Sort, and J. Nogues, *Phys. Rev. B* 79, 014436 (2009).

[24] W. Jung, F. J. Castano, and C. A. Ross*, Phys. Rev. Lett.* 97, 247209 (2006).

[25] J. Wu, D. Carlton, J. S. Park, Y. Meng, E. Arenholz, A. Doran, A. T. Young, A. Scholl, C. Hwang, H. W. Zhao, J. Bokor, Z. Q. Qiu. *Nature Phys.* 7, 303–306 (2011).

[26] G.-W. Chern, H. Youk, and O. Tchernyshyov, J. Appl. Phys. 99, 08Q505 (2006)

[27] R. Hertel and C. M. Schneider, *Phys. Rev. Lett.* 97, 177202 (2006)

[28] O. A. Tretiakov and O. Tchernyshyov, *Phys. Rev. B* 75, 012408 (2007)

[29] T. Shinijo, T. Okuno, R. Hassdorf, K. Shigeto, T. Ono, *Science*, 289, 5481 (2000).

[30] S. K. Kim and O. Tchernyshyov, *Phys. Rev. B* 88, 174402 (2013).

[31] Thiaville, A. and Miltat, J. *Topology in Magnetism* (eds Zang, J., Cros, V. & Hoffmann, A.) 62 (Springer International Publishing, Cham, 2018).

[32] Im M., Fischer P., Yamada K., Sato T., Kasai S., Nakatani Y., Ono T., *Nat Commun* 3, 983 (2012).

[33] S. B. Choe, Y. Acremann, A. Scholl, A. Bauer, A. Doran, J. Stöhr, and H. A. Padmore, *Science* 304, 420 (2004).

[34] S. Bohlens, B. Krüger, A. Drews, M. Bolte, G. Meier, and D. Pfannkuche. *Appl. Phys. Lett.* 93, 142508 (2008).

[35] A. B. Butenko, A. A. Leonov, A. N. Bogdanov, and U. K. Rößler *Phys. Rev. B* 80, 134410 (2009).

[36] Y. M. Luo, C. Zhou, C. Won, and Y. Z. Wu, *AIP Adv.* 4, 047136 (2014).

[37] B. Van Waeyenberge, A. Puzic, H. Stoll, K. W. Chou, T. Tyliszczak, R. Hertel, M. Fähnle, H. Brückl, K. Rott, G. Reiss, I. Neudecker, D. Weiss, C. H. Back, G. Schütz. *Nature* 444, 461–464 (2006).

[38] R. Hertel, S. Gliga, M. Fähnle, and C. M. Schneider, *Phys. Rev. Lett*. 98, 117201 (2007).

[39] A. Vansteenkiste, K. W. Chou, M. Weigand, M. Curcic, V. Sackmann, H. Stoll, T. Tyliszczak, G. Woltersdorf, C. H. Back, G. Schütz, B. Van Waeyenberge. *Nature Phys* 2009, 5, 332–334.

[40] E. Feldtkeller, Z. Angew. *Phys*. 19, 530 (1965).

[41] W. Döring, *J. Appl. Phys.* 39, 1006 (1968).

[42] A. Thiaville, J. M. García, R. Dittrich, J. Miltat, T. Schrefl, *Phys. Rev. B* 67, 094410 (2003).

[43] C. Donnelly, M. Guizar-Sicairos, V. Scagnoli, S. Gliga, M. Holler, J. Raabe, L. J. Heyderman, *Nature* 547, 328–331 (2017).

[44] P. Milde, D. Köhler, J. Seidel, L. M. Eng, A. Bauer, A. Chacon, J. Kindervater, S. Mühlbauer, C. Pfleiderer, S. Buhrandt, C. Schütte, A. Rosch, *Science* 340, 1076 (2013).

[45] A Wachowiak, J. Wiebe, M. Bode, O. Pietzsch, M. Morgenstern, R. Wiesendanger, *Science* 298, 5593 (2002).

[46] S. Brems, K. Temst, C. V. Haesendonck, *Phys. Rev. Lett.* 99, 067201 (2007).

[47] I. L. Guhr, O. Hellwig, C. Brombacher, M. Albrecht, *Phys. Rev. B* 2007, 76, 064434.

[48] Hans J. Hug, B. Stiefel, P. J. A. van Schendel, A. Moser, R. Hofer, S. Martin, and H.-J. Güntherodt, *J. Appl. Phys.* 83, 5609 (1998).

[49] Tony Alvarez*,* Sergei V. Kalinin*, and* Dawn A. Bonnell, *Appl. Phys. Lett*. 78, 1005 (2001).

[50] A. Vansteenkiste, J. Leliaert, M. Dvornik, M. Helsen, F. Garcia-Sanchez, B. Van Waeyenberge, *AIP Advances* 4, 107133 (2014).

[51] K. Yu. Guslienko, V. Novosad, Y. Otani, H. Shima, K. Fukamichi, *Appl. Phys. Lett.* 78, 3848 (2001).

[52] A. Hubert and R. Schäfer, *Magnetic Domains: The Analysis of the Magnetic Microstructures*, corrected 3rd printing 2005 ed. Springer-Verlag, Berlin, (1998).

[52] H. Kronmuller, Z. Phys. 168, 478 (1962).

[53] R. P. Cowburn, D. K. Koltsov, A. O. Adeyeye, M. E. Welland, and D. M. Tricker, *Phys. Rev. Lett*. 83, 1042 (1999).

[54] M. Noske, H. Stoll, M. Fähnle, R. Hertel, G. Schütz, *Phys. Rev. B* 91, 014414 (2015).

[55] R. Salikhov, A. Alekhin, T. Parpiiev, T. Pezeril, D. Makarov, R. Abrudan, R. Meckenstock, F. Radu, M. Farle, H. Zabel, and V. V. Temnov, *Phys. Rev. B* 99, 104412 (2019).

[56] M. Hayashi, L. Thomas, C. Rettner, R. Moriya, S. S. P. Parkin, *Nature Phys.* 3, 21–25 (2007).

[57] Sluka V., Schneider T., Gallardo R. A., Kákay A., Weigand M., Warnatz T., Mattheis R., Roldán-Molina A., Landeros P., Tiberkevich V., Slavin A., Schütz G., Erbe, Deac A., Lindner J., Raabe J., Fassbender J., Wintz S., *Nat. Nanotechnol*. 14, 328–333 (2019).

[58] N. Sato, K. Schultheiss, L. Körber, N. Puwenberg, T. Mühl, A. A. Awad, S. S. P. K. Arekapudi, O. Hellwig, J. Fassbender, and H. Schultheiss, *Phys. Rev. Lett.* 123, 057204 (2019).

[59] Im, M., Han H. S., Jung M. S., Yu Y. S., Lee S., Yoon S., Chao W., Fischer P., Jung-Il Hong, Lee K. S., *Nat. Commun.* 10, 593 (2019).

[60] Okuno, T., Mibu, K., & Shinjo, T. *Journal of Applied Physics, 95(7), 3612–3617* (2004).

[61] Radu F and Zabel H 2008 Exchange Bias Effect of Ferro-/Antiferromagnetic Heterostructure (Berlin: Springer).

[62] M. S. Lund, W. A. A. Macedo, K. Liu , J. Nogués , I. K. Schuller and C. Leighton , *Phys. Rev. B: Condens. Matter,* 66, 054422 (2002).

[63] J. N. Rigue, F. Beck, A. M. H. de Andrade, P. R. Kern, J. V. Siqueira and M. Carara. *IEEE Mang. Lett.* 6 (3800204) pp.1–4 (2015).

[64] Yamaoka, T., Mekata, M., Takaki, H. *J. Phys. Soc. Japan,* 36, 438–444 (1974).

[65] A. Kohn, A. Kovács, R. Fan, G. J. McIntyre, R. C. C. Ward, J. P. Goff, *Sci Rep*., 3, 2412 (2013).

[66] L. Néel, C. R. Hebd. Seances, *Acad. Sci*., 255, 1676 (1962).

[67] J. Moritz, F. Garcia, J.C. Toussaint, B. Dieny, J.P. Nozières, *Europhys. Lett*., 65, 123 (2004).

[68] X. Ma, G. Yu, S. A. Razavi, S. S. Sasaki, X. Li, K. Hao, S. H. Tolbert, K. L. Wang, Xiaoqin Li, Phys. Rev. Lett. 119, 027202 (2017).

[69] M. Noske, H. Stoll, M. Fähnle, R. Hertel, G. Schütz, *Phys. Rev. B* 91, 014414 (2015).

[70] M. Fitzsimmons, B. Kirby, S. Roy, Z.-P. Li, I. Roshchin, S. Sinha and I. Schuller, *Phys. Rev. B* 75, 214412 (2007).

[71] S. Brück, G. Schütz, E. Goering, X. Ji and K. Krishnan, *Phys. Rev. Lett.,* 2008, 101, 126402 (2008).

[72] H. Ohldag, A. Scholl, F. Nolting, E. Arenholz, S. Maat, A. Young, M. Carey and J. Stöhr, *Phys. Rev. Lett*., 91, 017203 (2003).

[73] Christian Holl, Marvin Knol, Marco Pratzer, Jonathan Chico, Imara Lima Fernandes, Samir Lounis & Markus Morgenstern. *Nat Commun* 11, 2833 (2020).

[74] J. M. García-Martín, A. Thiaville, J. Miltat, T. Okuno, L. Vila, L. Piraux. *J. Phys D: Appl. Phys.,* 37 965-972 (2004).

[75] N.A. Usov, S.E. Peschany. Journal of Magnetism and Magnetic Materials 118, L290–L294 (1993).

[76] Peter Fischer, Mi-Young Im, Shinya Kasai, Keisuke Yamada, Teruo Ono, and André Thiaville. *Phys. Rev. B* 83, 212402 (2011)

[77] A. Thiaville, J. Miltat, J.M. García, Magnetic force microscopy. Images of nanostructures and contrast modeling, edited by H. Hopster, H.P. Oepen, Springer, Berlin, pp. 225–251 (2005).

[78] Mironov, V.L., Yermolaeva, O.L. *J. Synch. Investig*. 1, 466–470 (2007).

[79] P. Kappenberger, S. Martin, Y. Pellmont, H. J. Hug, J. B. Kortright, O. Hellwig, and Eric E. Fullerton. *Phys. Rev. Lett*. 91, 267202 (2003).

[80] I. Schmid, M. A. Marioni, P. Kappenberger, S. Romer, M. Parlinska-Wojtan, H. J. Hug, O. Hellwig, M. J. Carey, and E. E. Fullerton. *Phys. Rev. Lett*. 105, 197201 (2010).

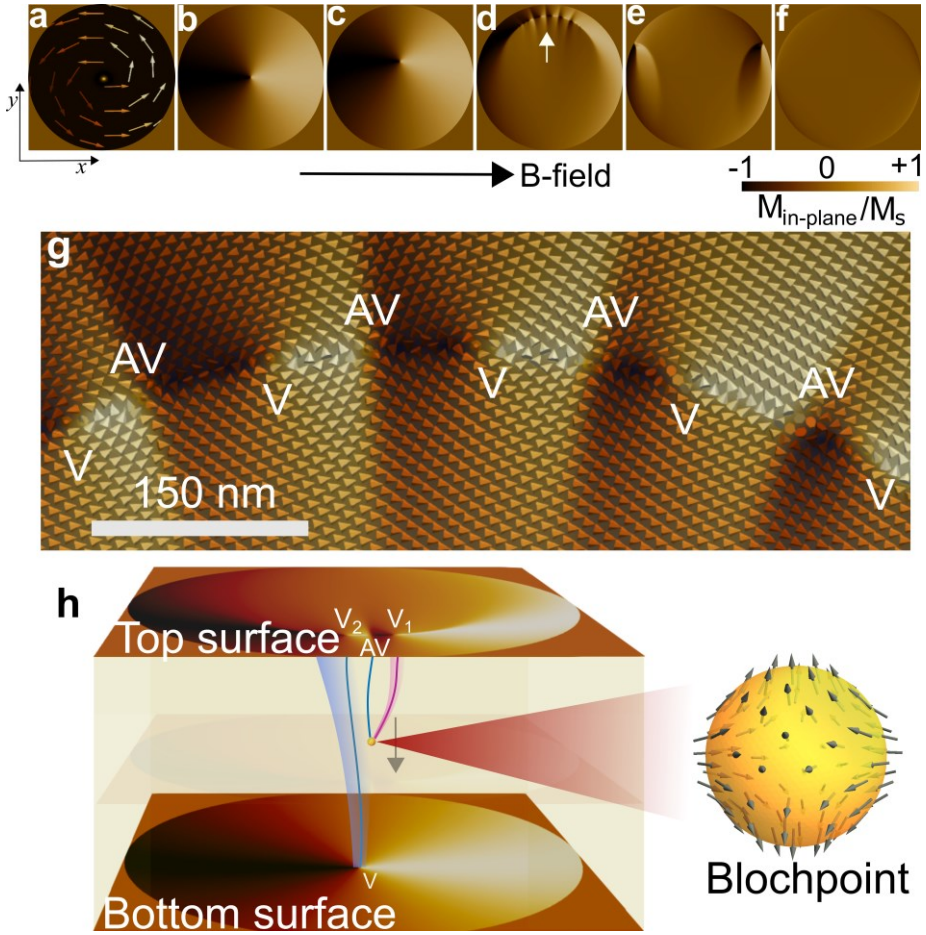

Figure 1. Magnetic vortex annihilation mediated by the creation and annihilation of V-AV pairs in static magnetic field obtained from micromagnetic simulation for a 2 μm disk diameter with handedness $c \cdot p = +1$. a) In-plane (IP) spin structure of the vortex with an out-of-plane (OOP) core polarization. (b-f) Vortex core deflection in the positive *y*-direction as a consequence of the applied B-field and subsequent creation of vortex-antivortex pairs (d),

followed by an edge vortex state (e) and saturation state (f). (g) Detailed spin structure of the V-AV pairs overlaid on the buckled IP spin texture from the region indicated with an arrow in (d). (h) Schematic for the injection and propagation mechanism of a BP through the film thickness. The original vortex V_1 (p = -1), and the newly nucleated vortex V_2 with opposite core polarization (p = +1). An antivortex with polarization p = +1 is created to separate the two vortex cores. Spiraling BP structure for q = +1 is shown as well.

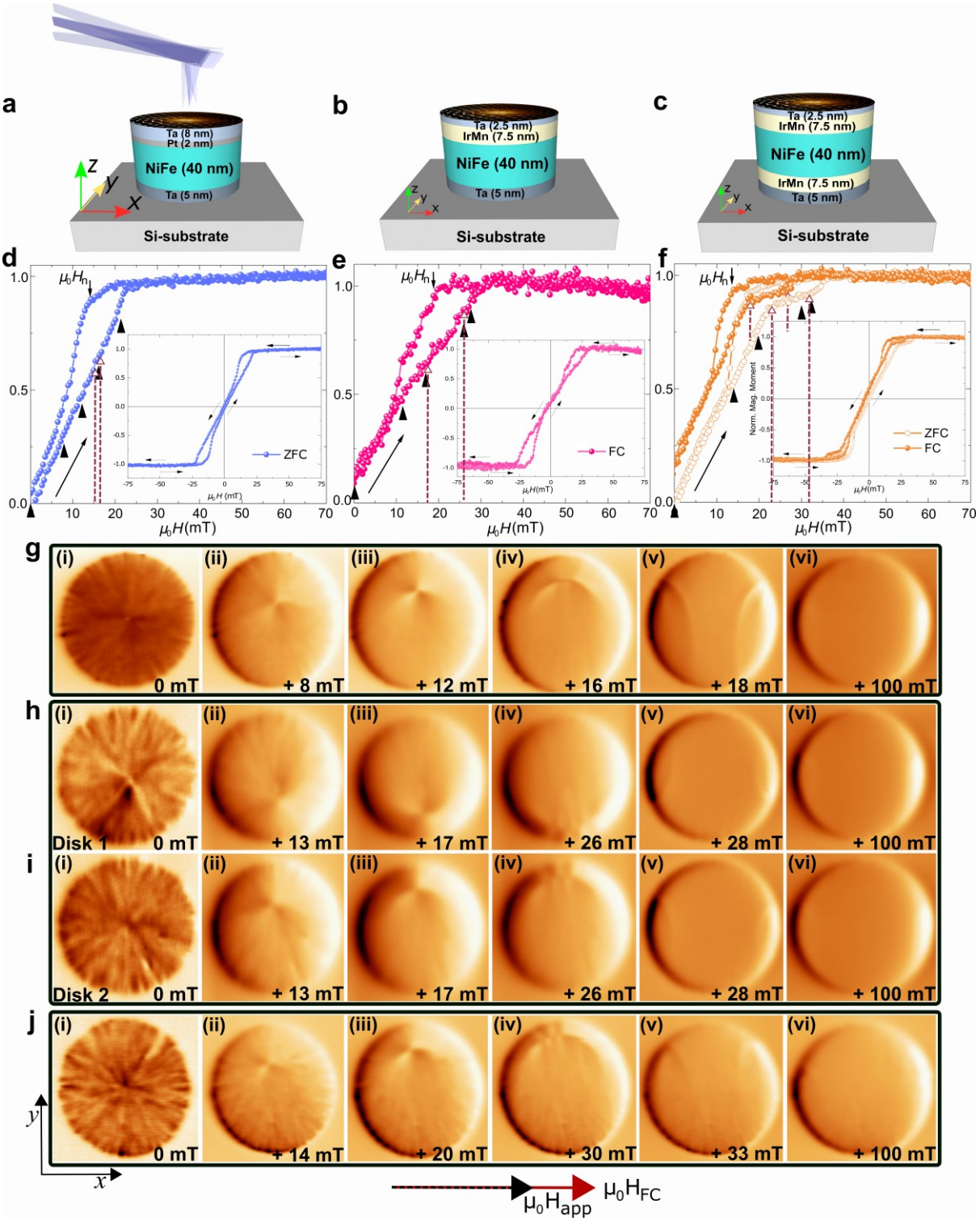

Figure 2. Disk structures and the corresponding hysteresis loops, and in-field Hr-MFM image sequences. (a-c) Disk structures with 4 µm diameter investigated in this study consisting of a simple FM, AFM/FM & AFM/FM/AFM, respectively. Scanning electron microscopy images of the patterned disk arrays are shown in supplementary figure S6. (d-f) Longitudinal MOKE hysteresis loop obtained at 300 K for the FM, AFM/FM & AFM/FM/AFM disk structures after

FC and ZFC as indicated. The full hysteresis loops are shown as an inset. The brown dashed arrow lines indicate the magnetic field region, where V-AV phases are stable for the three different structures shown. Black triangles indicate the magnetic field values at which the MFM images were obtained. In-field MFM image sequences for the simple FM case g(i-vi), the AFM/FM case for disk 1 h(i-vi), and disk 2 i(i-vi), and the AFM/FM/AFM case j(i-vi) are shown.

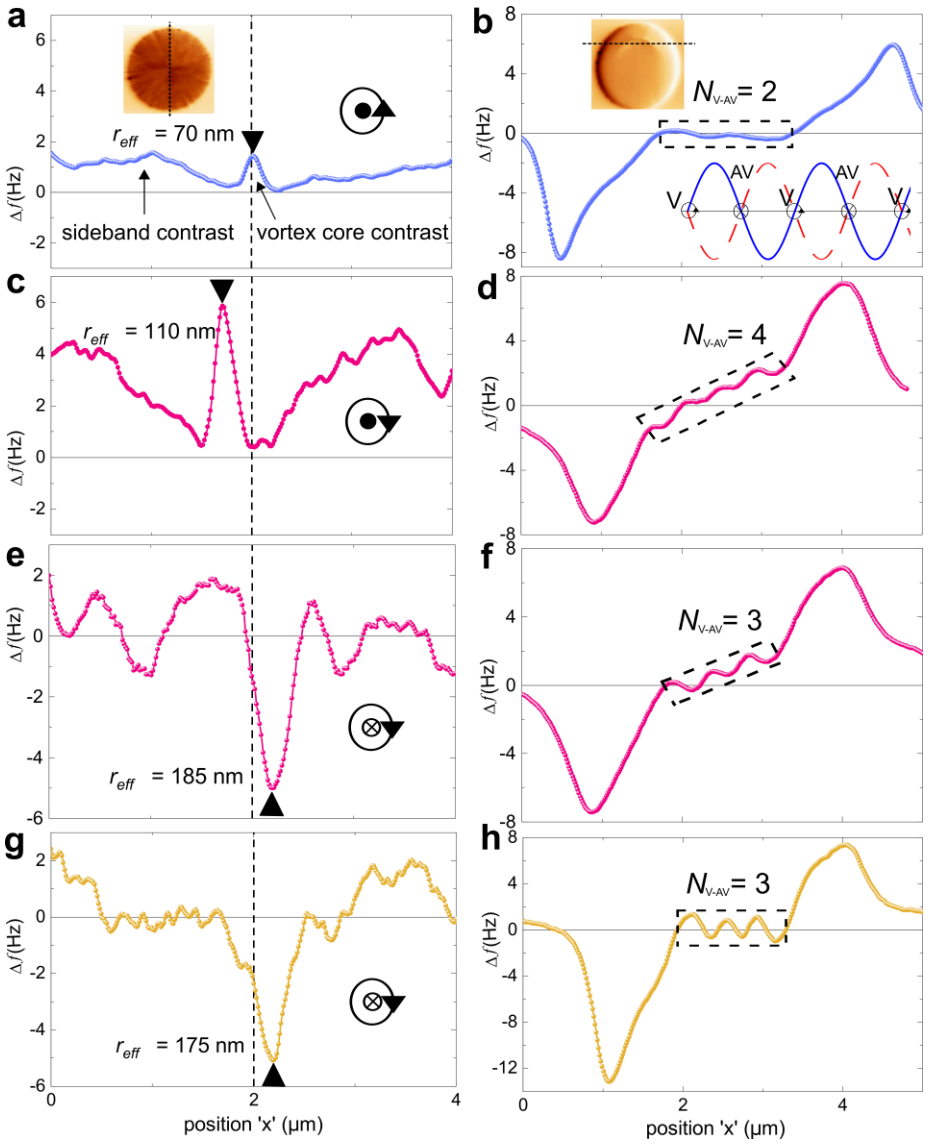

Figure 3. Line profile extracted from the MFM images for the ground (vortex) state at remanence and the in-field V-AV state in FM and FM/AFM and AFM/FM/AFM disks. (a and b) Line profile for the vortex core and the buckled spin structure for the FM disk structure. The line profile is extracted from the position shown in the inset MFM images. (c and d) The line profile for the AFM/FM case, for disk 1 (cp = -1), and (e and f) disk 2 (cp = +1) are extracted from the MFM images shown in figure 2 (h) (i & iv) and (i) (i & iv) respectively. (g and h) The line profile for the AFM/FM/AFM case, extracted from the Figure 2 j(i and iv). Black triangles indicate the vortex core position on the 4 μm disk. The dashed rectangles indicate the magnetic contrast ($\Delta f(Hz)$) corresponding to the buckled (V-AV) spin texture. The inset in (b) shows a guide to the eye for extracting the number of V-AV pairs from the line profile of the buckled spin texture.

Table 1. Summary of the various characteristic properties of the magnetic vortex structures obtained experimentally from the combination of in-field HR-MFM imaging and nano-MOKE magnetometry.

Layer structure	*c·p*	Effective core radius r_{eff} [nm]	Core displacement Δd_{core} [nm]	$\mu_0 H_n$ [mT] (±1 mT)	$\mu_0 H_a$ [mT] (±1 mT)	V-AV pairs N_{V-AV}	V-AV state field range [mT]	$\mu_0 H_{eb}$ [mT]	ΔE_{eb} [μJ/m^2]	V-AV state
Ta (8 nm)/Pt (2 nm)/**NiFe (40 nm)**/Ta (5 nm) /Substrate	+1	70	<6	14	15	2	<2	-	-	Transformed to *edge vortex state* upon repeating the in-field MFM scan at ~16 mT
Ta (2.5 nm)/**IrMn (7.5 nm)/NiFe (40 nm)**/Ta (5 nm) /Substrate	-1||+1	110||185	270||210	18	26	4||3	8	-2.5	77.8	Stable beyond 24 hours at ~26 mT
Ta (2.5 nm)/**IrMn (7.5 nm)/NiFe (40 nm)/ IrMn (7.5 nm)**/Ta (5 nm) /Substrate	+1	175	160	14 (FC) 18(ZFC)	27(FC) 31(ZFC)	3	10(FC) 11(ZFC)	-4.5	140	Stable beyond 24 hours at ~30 mT

Note: The FC and ZFC refer to the field cooled and zero field states.